Journal of Geophysical Research: Earth Surface

Supporting Information for:

Stochastic Simulations of Bed Topography Constrain Geothermal Heat Flow and Subglacial Drainage near Dome Fuji, East Antarctica

Calvin Shackleton[1*], Kenichi Matsuoka[1], Geir Moholdt[1], John Paden[2], Brice Van Liefferinge[1]

[1] Norwegian Polar Institute, Fram Senteret, Tromsø, Norway, 9296
[2] Center for Remote Sensing of Ice Sheets (CReSIS), The University of Kansas, Lawrence, KS, USA, 66045
**calvin.shackleton@npolar.no*

Contents of this file

Additional Supporting Information (Files uploaded separately)

Captions for Movies S1 to S2

Introduction

Supporting text S1 provides additional details for individual ice thickness data sources (S1.1), the data calibration (S1.2), and crossover analysis (S1.3). S2 provides further detail on the stochastic simulation of bed topography (see section 2.2 in main text), including software and tools used (S2.1) and geostatistical model development and implementation into simulations (S2.2). S3 is an extended description of the results, including validation of simulated bed results (S3.1), geothermal heat flow models and topographic adjustments (S3.2), and model parameters for the bed roughness and uncertainty analysis (S3.3).

Text S1. Individual data sources and data standardization

S1.1 Ice-thickness data sources

The sources for all ice-thickness data used in this study are listed in Table S1, and the following text outlines any additional details and processing of available data:

CReSIS: Data are geolocated radar data (echograms).

JARE*:* Ice-thickness data collected between 1992 and 2008 (*JARE33-49)* had been calibrated to *JARE59-60* surveys based on crossover error analysis (Tsutaki et al., 2022). We combined the older radar survey JARE 33-54 data collected between 1992 and 2013 and filtered out data if there were newer data from more recently conducted surveys (*CReSIS, JARE59-60, AWI*) within 500 m.

Bedmap2: Gridded ice-thickness data were extracted from the Bedmap2 ice-thickness grid using the survey coverage mask. Data were filtered out if there were any survey data (CReSIS, JARE33-60, AWI) within 10 km. This procedure yields only grid values based on data from the Soviet Antarctic Expedition (Kapitsa, 1964).

***BedMachine*:** Gridded ice-thickness data were extracted from the BedMachine v2 ice-thickness grid by sampling across the Dome Fuji region at a uniform 2 km spacing to yield 6752 data points. The sampled data were then filtered out if they were within 10 km of radar-derived ice-thickness measurements (*CReSIS, JARE33-60, AWI, Bedmap2*). BedMachine v3 was released close to the end of our experiments, however, analysing differences between v3 and v2 in the Dome Fuji region at our 6752 sample points yielded differences with mean 0.6 m and standard deviation 9.2 m, suggesting negligible impacts on our results.

The study region is from 596 km to 1020 km Easting, 816 km to 1240 km Northing, on a Polar Stereographic projection parallel to 71°S (EPSG: 3031). We added a 100 km buffer to this region before clipping available data to prevent too few data being available close to the region boundary when running the stochastic simulations. Ice-thickness measurement data were then decimated to a minimum 100 m spacing using a median reduction filter. This removes some surplus data at the chosen resolution of 500 m and also reduces the likelihood of closely spaced measurements with large inconsistencies in thickness which could lead to misrepresented topographic roughness.

***Table S1**: Source of the radar data used for generating subglacial topography grids.*

Institute/ data origin	Survey/Project name	Acquisition date	Source/DOI/key reference
Alfred Wegener Institute (AWI)	Geodynamic Evolution of East Antarctica (GEA)	2013-2015	(Eagles et al., 2021) https://doi.org/10.1594/PANGAEA.938357
Alfred Wegener Institute (AWI)	Oldest Ice Reconnaissance (OIR)	2016-2017	(Eisen et al., 2020) https://doi.pangaea.de/10.1594/PANGAEA.920619
British Antarctic Survey	Bedmap2; Soviet Antarctic Expedition (SAE) measurements	1964	(Fretwell et al., 2013): grid https://secure.antarctica.ac.uk/data/bedmap2/ (Kapitsa, 1964): data points
Centre for Remote Sensing of Ice Sheets (CReSIS), University of Kansas	RDS 2018 Antarctica Ground	2018-2019	(Rodriguez-Morales et al., 2020) https://ops.cresis.ku.edu/
NASA	Bedmachine	-	(Morlighem et al., 2020) https://nsidc.org/data/nsidc-0756/versions/3
National Institute of Polar Research (NIPR)	Japanese Antarctic Research Expedition (JARE) 33	1992-1993	(Tsutaki et al., 2021a) https://doi.org/10.17592/001.2021110902
	JARE 37	1996-1997	(Tsutaki et al., 2021b) https://doi.org/10.17592/001.2021110903
	JARE 40	1999-2000	(Tsutaki et al., 2021c) https://doi.org/10.17592/001.2021110904
	JARE 49	2007-2008	(Tsutaki et al., 2021d) 179 MHz: https://doi.org/10.17592/001.2021110905 (Tsutaki et al., 2021e) 60 MHz: https://doi.org/10.17592/001.2021110906
	JARE 54	2012-2013	(Tsutaki et al., 2021f) https://doi.org/10.17592/001.2021110907
	JARE 59	2017-2018	(Tsutaki et al., 2021g) https://doi.org/10.17592/001.2021110908; (Tsutaki et al., 2021h) https://doi.org/10.17592/001.2021110909
	JARE 60	2018-2019	(Tsutaki et al., 2021i) https://doi.org/10.17592/001.2021110910

S1.2 Calibration and standardization of ice-thickness measurements

Ice-thickness measurements were compiled from various sources (Table S1) and standardized if required. The two-way travel time (TWT) for transmitted radio wave reflections from the ice-surface minus the ice bottom were converted to ice-thickness (h) using:

$$h = \frac{TWT * V_{ice}}{2}$$

where V_{ice} is the propagation speed of radar waves in ice. To standardize these data from different sources we used a single V_{ice} = 1.69 x 10^8 m s^{-1} which was used by Tsutaki et al. (2022) taking into account the ice properties observed in the Dome Fuji ice core. Applying this parameterization across all radar datasets also gives ice thicknesses within 500 m of the drilling site (Table S2) that are close to the estimate of 3028 ± 15 m at the core site (Fujita et al., 2006).

Table S2: *Ice-thicknesses within 500 m of the DF1 core site.*

Survey	Data Points	Mean (m)	Median (m)	STD (m)
AWI	56	3033.5	3036.2	11.2
CReSIS	51	3013.3	3013.0	14.7
JARE59	474	3017.0	3015.0	15.7
JARE49	1	3036.0	3036.0	-
All surveys	582	3018.3	3017.0	16.1

AWI: A firn correction of +10 m was removed from the OIR and GEA ice-thickness data and TWT was calculated from ice-thicknesses using the wave propagation speed of 1.67 x 10^8 used by Karlsson et al., (2018). We then used a wave propagation speed of 1.69 x 10^8 m s^{-1} to standardise ice-thickness estimates.

CReSIS: We calibrated for observed time 0 variability along each CReSIS survey line by tracking TWT for the first peak in returned power within the upper 0.7 µs and applying a gaussian smoothing function in a horizontal moving window of 500 data points (Figures S1, S2). The vertical search window was chosen after manual inspection of each survey line showed the first peak within the upper 0.7 µs, which we assumed to be the ice surface. The TWT to ice bottom (i.e., ice-bed interface) was picked using semi-automated algorithms on newly processed echograms. Radar echograms were manually inspected, and layer picks adjusted using manual control points where necessary using the CReSIS Toolbox ("CReSIS Toolbox," 2021) working on MATLAB. The ice bottom TWT was subtracted from ice surface TWT to give ice thickness. TWT was converted to depth in meters using a wave propagation speed of 1.69 x 10^8 m s^{-1}.

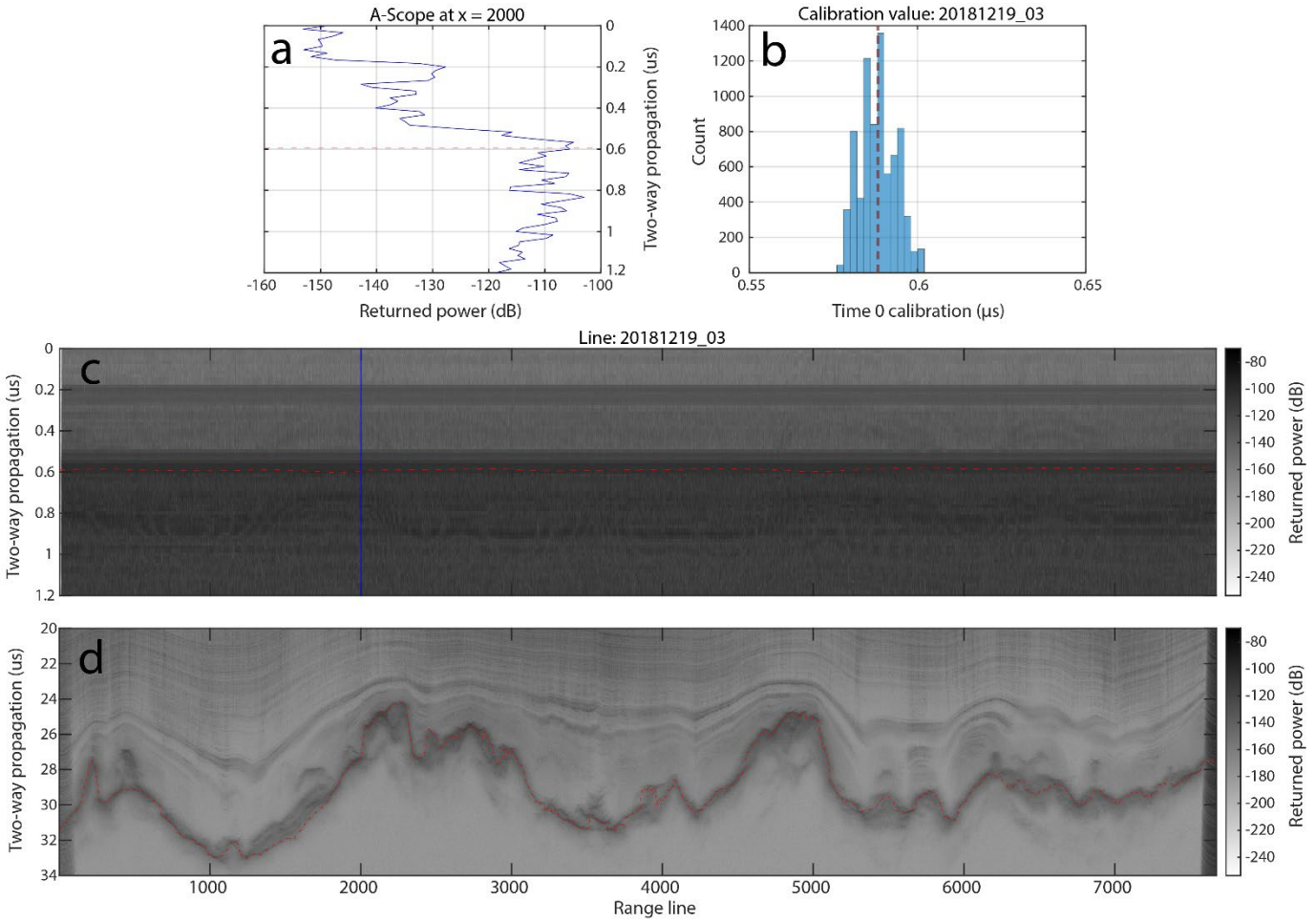

Figure S1: *Time 0 calibration results for CReSIS ice-thickness data, for profile 20181219_03.* ***a)*** *Returned power (dB) plotted against TWT (µs) at position x = 2000 (blue line) on the echogram. TWT for the first peak is drawn in red.* ***b)*** *Distribution of TWTs to the first peak along this profile. Vertical red dashed line shows mean value.* ***c - d)*** *Echograms showing the ice surface reflection at 0 – 1.2 µs, and the bed reflection at 20 – 34 µs. The red line in panel* ***c*** *shows the calibrated ice sheet surface and the red curves in panel* ***d*** *show the picked bed reflector.*

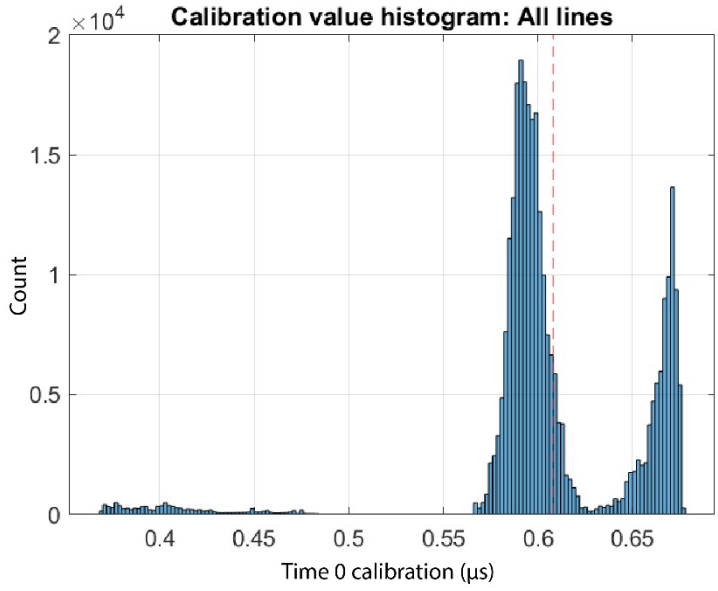

Figure S2: *Distribution for all Time 0 calibration results for all CReSIS radar profiles and the mean value (red line).*

S1.3 Crossover analysis

A crossover analysis was conducted between the CReSIS radar survey and three other radar surveys (JARE59, JARE60, and AWI OIR). AWI GEA data have no crossover points with CReSIS data. Measurements close to the survey basecamp with unstructured survey profiles were masked out in a 6 x 3 km region centred at 844125 Easting, 1037460 Northing. The XY locations of survey track crossover points was calculated, then a 30 m buffer was used to extract ice-thickness measurements and calculate mean values per survey. The crossover differences were calculated as CReSIS ice-thickness measurements minus JARE59, JARE60, AWI OIR measurements (Figure S3a), yielding respective median differences of 3 m, 18 m, and -1 m. The spatial distribution of differences (Figure S3b) does not show clustering of anomalously large or small differences and the median biases we observed were quite close to zero, so we chose not to calibrate the data further.

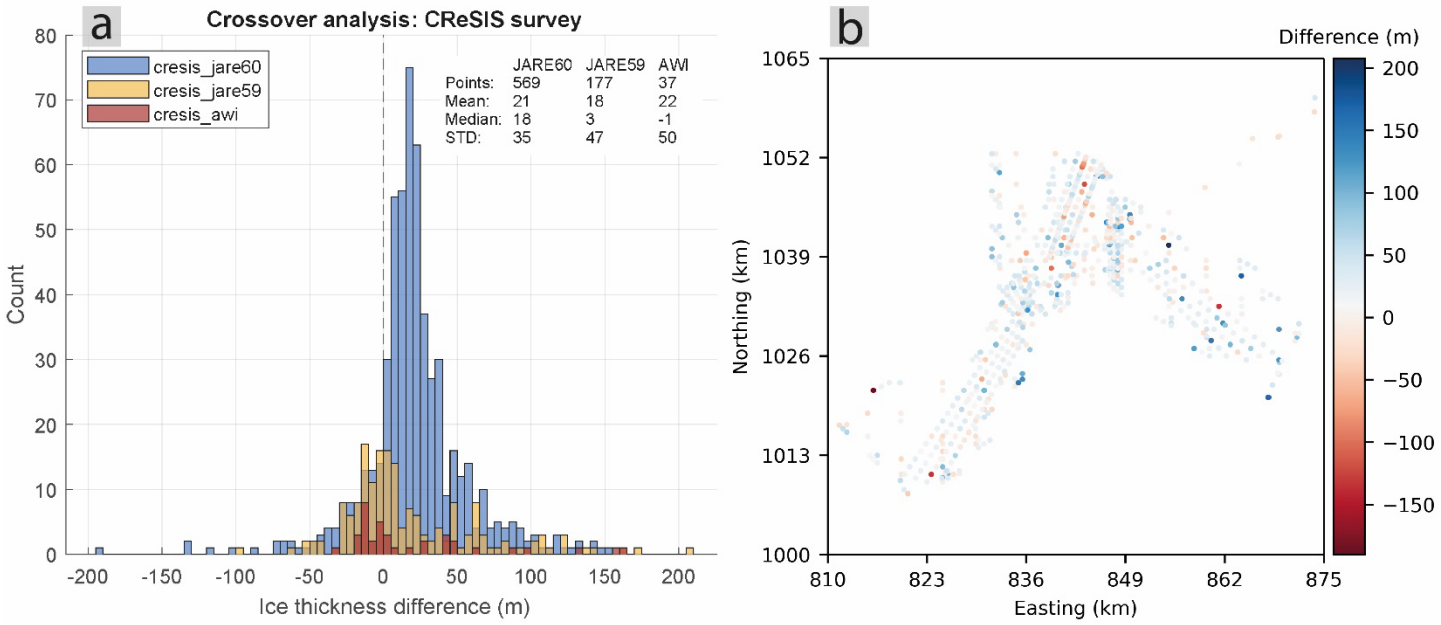

Figure S3: *Crossover analysis.* ***a)*** *The distribution of ice-thickness measurement differences between the CReSIS radar survey and the AWI OIR, JARE 59, and JARE 60 surveys.* ***b)*** *Spatial distribution of survey measurement differences.*

Text S2. Stochastic simulation of bed topography

S2.1 Software and tools

We used Python 3.9.7 to conduct the analysis, with packages for data manipulation, raster processing and analysis (numpy, rasterio, pandas, rioxarray, rasterstats, xarray, pyproj, cartopy, scipy). We also used and adapted tools for geospatial/ geostatistical analysis and stochastic methods from the following open-source python packages: Verde (Uieda, 2018), GeoStatsPy (Pyrcz et al., 2021), SciKit GStat (Mälicke et al., 2021), and GStatSim (Mackie et al., 2022). Specifically, the Verde 'BlockReduce' function was used for data decimation with median filter. From GeoStatsPy, the 'nscore' function was used to compute normal scores for ice-thickness data, 'gamv' function was used to compute experimental semivariograms, and 'vmodel' used to create exponential variogram models. From the GlacierStats package (MacKie et al., 2022) we used the 'okrige_sgs' function for sequential gaussian simulation algorithms based on ordinary kriging and several other tools during preliminary data analysis and experiments.

S2.2 Geostatistical model development and implementation

Decimated ice-thickness data were normalized using a normal score transformation so that the values fit a standard Gaussian distribution (Deutsch & Journel, 1997). Weighting parameters were stored to later transform values back into ice-thickness. Experimental semivariograms for ice-thickness data were calculated to find expected variance between data points as a function of distance. In preliminary experiments semivariograms were obtained for 4 azimuthal ranges of 45 degrees with centres at 0, 45, 90, and 135 degrees. We did not observe significant anisotropy in ice-thickness measurements (Figure S4a). We also simulated ice-thickness using regional semivariograms and models for up to 5 regions (Figure S4b) within the study area shown in Figure 1. Despite some difference between the central region (DF4 labelled in Figure S4b) and surrounding regions (DF0, DF1, DF2, DF3 and DF4) we found after fitting an exponential model that parameters were not different enough with this procedure to justify the extra time taken to run the analysis with region-specific statistical models. We therefore proceeded using an isotropic semivariogram, accepting a slight bias towards regionally higher roughness which we find appropriate given the ensemble-analysis approach. Based on the distance between survey profiles (0.5 – 15 km), maximum distance between ice-thickness data (15 km) and the scale of major topographic features (10's of km) we calculated an isotropic experimental semivariogram with maximum lag of 80 km at lag intervals of 500 m (Figure S5).

An exponential statistical model was fit to the experimental semivariogram using a Trust Region Reflection least squares function, with resulting range = 80000, sill = 1, nugget = 0 (Figure S5), representing the variance between ice-thickness measurements as a function of distance. The statistical model was used in SGS to estimate local mean and variance for a Gaussian probability density function at un-surveyed locations using ordinary kriging. A value is selected at random from this distribution to simulate the ice-thickness, and the grid cell is added to conditioning data and included in subsequent calculations. In initial experiments we examined the algorithm run time for different influencing factors, including number of conditioning data points for the probability distribution, the search radius around un-surveyed grid cells for conditioning data, the output grid cell size (between 0.1 and 5 km), the study region boundary, and the level of data decimation. We chose parameters of 40 nearby data points within a search radius of 30 km for our optimum experiment, yielding simulated topography with 500 m grid cells that kept the algorithm run times to an acceptable level.

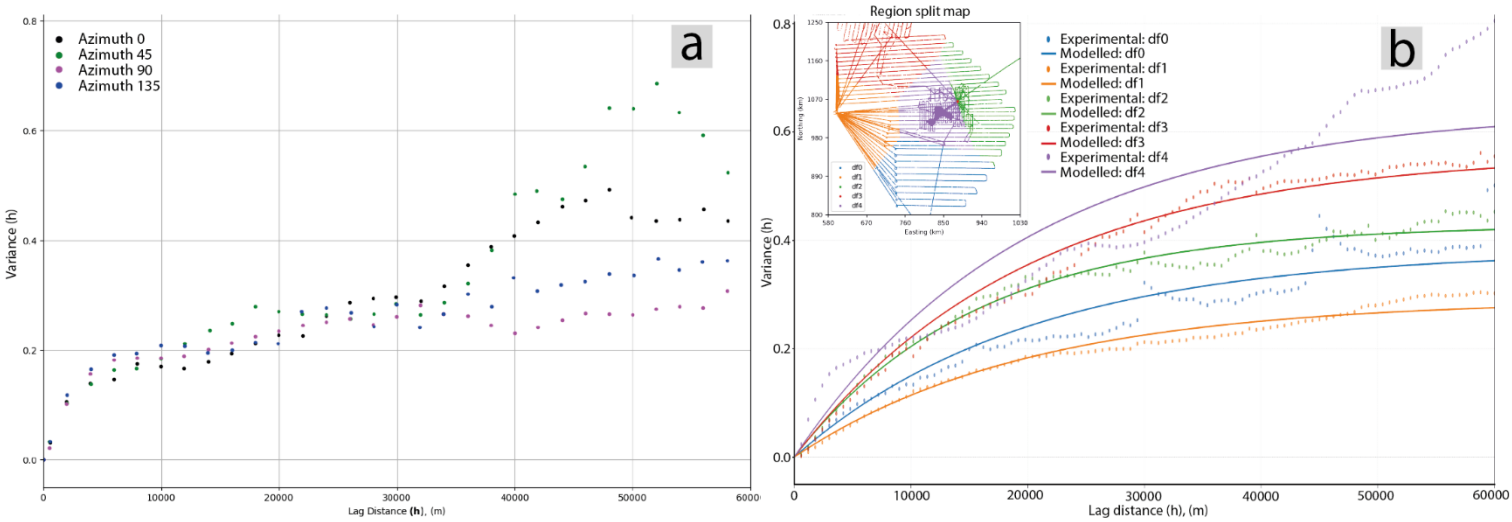

Figure S4: *Experimental semivariograms and variogram models.* ***a)*** *Variograms across 4 azimuthal ranges for lag distance intervals of 2 km. Differences in variance are larger for lag distances over 40 km, but similar variance is observed for the different azimuths when the lag distance is less than 30 km which is the target range of this study.* ***b)*** *Regionally calculated experimental semivariograms and statistical models.*

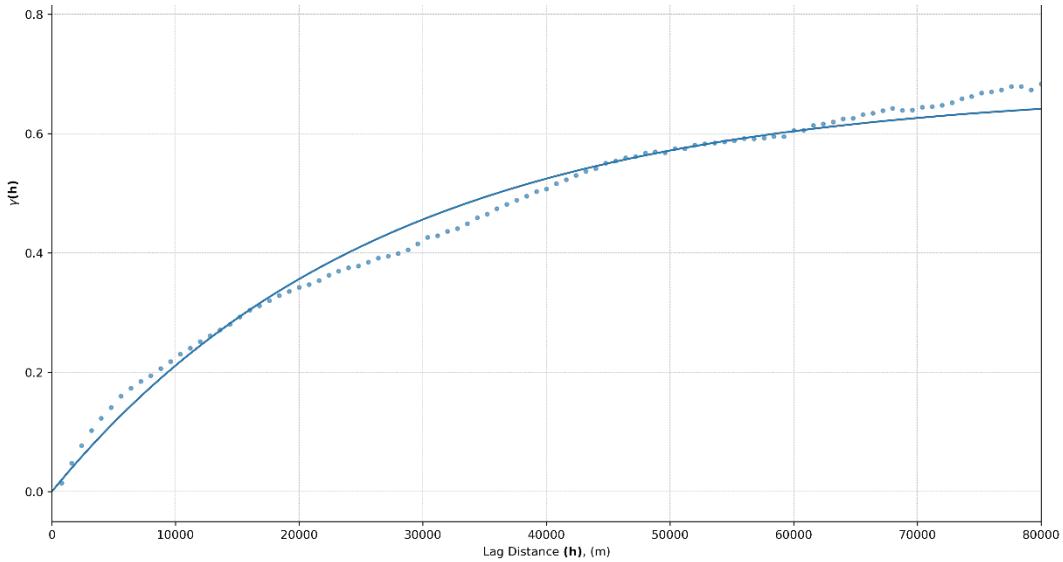

Figure S5: *Optimum experiment exponential model (blue line) fit to the experimental semivariogram for ice-thickness data (blue dots).*

Text S3. Results

All 100 simulated bed-topography, ice-thickness, and topographic geothermal heat flow adjustment grids are available at the Norwegian Polar Data Centre (https://doi.org/10.21334/npolar.2023.dbd63194). The results are in raster format (.tiff) in an Antarctic Polar Stereographic (EPSG: 3031) coordinate system. The spatial extent is 596000 m to 1020000 m Easting and 816000 m to 1240000 m Northing with cell size 500 m x 500 m (848 columns, 848 rows). Ice-thicknesses are provided in meters and bed elevations are in meters referenced to the WGS84 Ellipsoid.

S3.1 Validation of simulated bed

Over the entire study region (719,104 cells), 6.4% of the grid (46,374 cells) contain ice-thickness measurements and 94% (43,600 cells) of these contain 30 or fewer measurements. Figure S6a shows the number of ice-thickness measurements per grid cell for $1 \leq n \leq 30$. The bias at around 15 measurements per grid cell is likely sourced from the sample rates along radar profiles which are 15 - 30 m for CReSIS, JARE60 and AWI OIR data. Every simulated ice-thickness grid in our ensemble was assessed for agreement with the full ice-thickness measurements dataset (i.e., measurement data before decimation). Figure S7 shows the distributions for these differences and correlation between measurement data and simulated ice-thickness grid value at the measurement location. The mismatches have a large standard deviation (σ = 51 m), although this is within the expected range considering the measurement variability observed within each grid cell (Figure S6b).

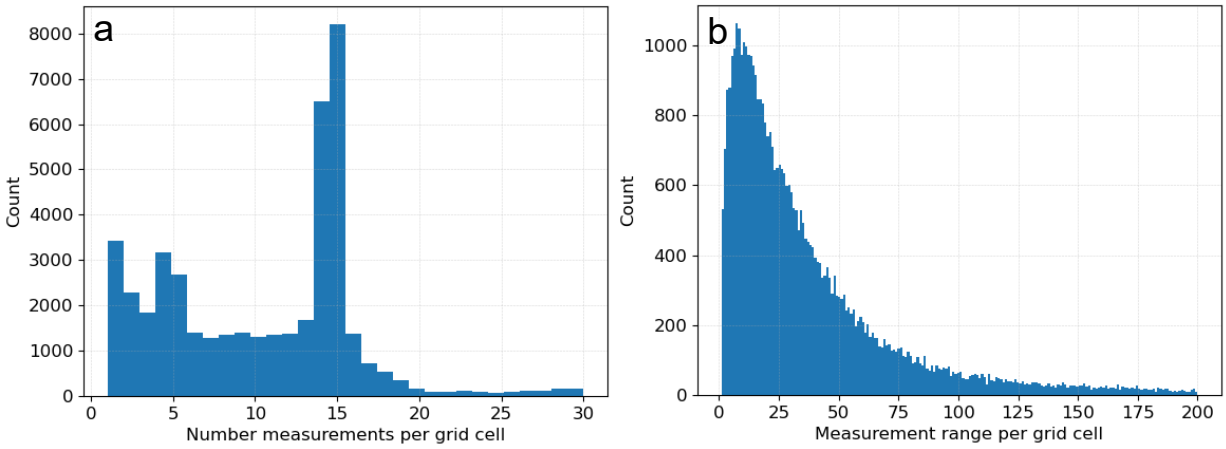

Figure S6: *Statistics for ice-thickness measurements contained within each 500 m x 500 m cell of our results grid.* ***a)*** *Number of measurements per grid cell.* ***b)*** *The difference between the highest and lowest measurement per grid cell.*

Bed roughness and topographic features are most reliable in regions with high measurement density and small distances between survey tracks. In regions with large spacings between survey lines, GHF adjustments cannot accurately reflect impacts at the scale of individual topographic features. However, regional spatial patterns of modification are realistic due to the consistency between interpolated values and measured local roughness characteristics. Beyond radar survey extents, for example outside AWI survey tracks (Figure 1a), the regional pattern and roughness characteristics of simulated subglacial topography reflect only the properties

of the BedMachine sample points. However, regularly-spaced 2 km sample points ensured little deviation from the streamline diffusion interpolations from Morlighem et al., (2020) and provided data in peripheral regions necessary to generate a contiguous grid.

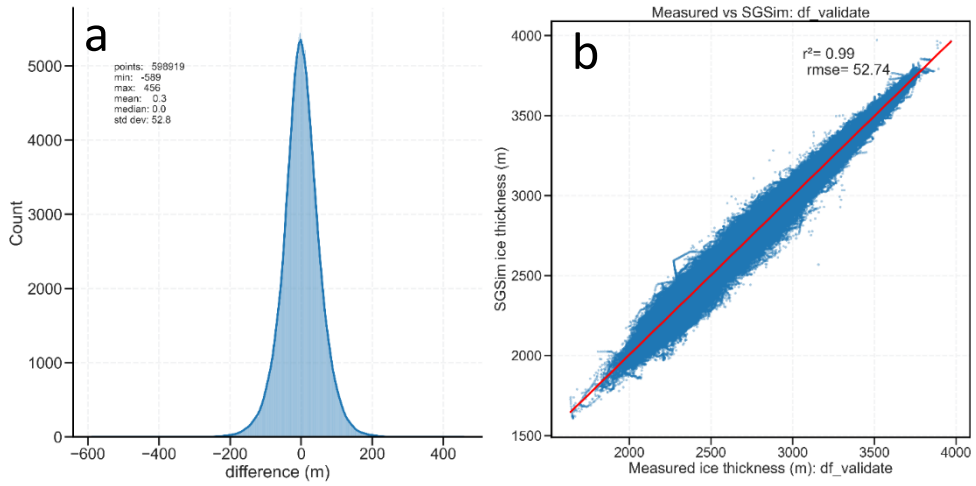

Figure S7: *Validation results for SGS result #001. a) Measured minus simulated difference distribution. b) measured ice-thickness plotted against simulated grid cell value.*

S3.2 Geothermal heat flow models and topographic adjustment

Figure S8 shows GHF in the Dome Fuji region for 7 different GHF models (Shen et al., 2020; Stål et al., 2020; An et al., 2015; Purucker, 2012; Losning et al., 2021; Martos et al., 2017; Burton-Johnson et al., 2020). Their distributions at native resolution are plotted in Figure 2d in the main text. The local GHF after topographic modification (G´) was calculated following Colgan et al. (2021):

$$G' = G\left(1 + \frac{\Delta G}{G}\right), \quad \text{(S1)}$$

where G = modelled large-scale GHF estimate. ΔG/G = GHF perturbation by an anomaly, which is the function calculated by equation 1 in the main text (*Section 2.3*).

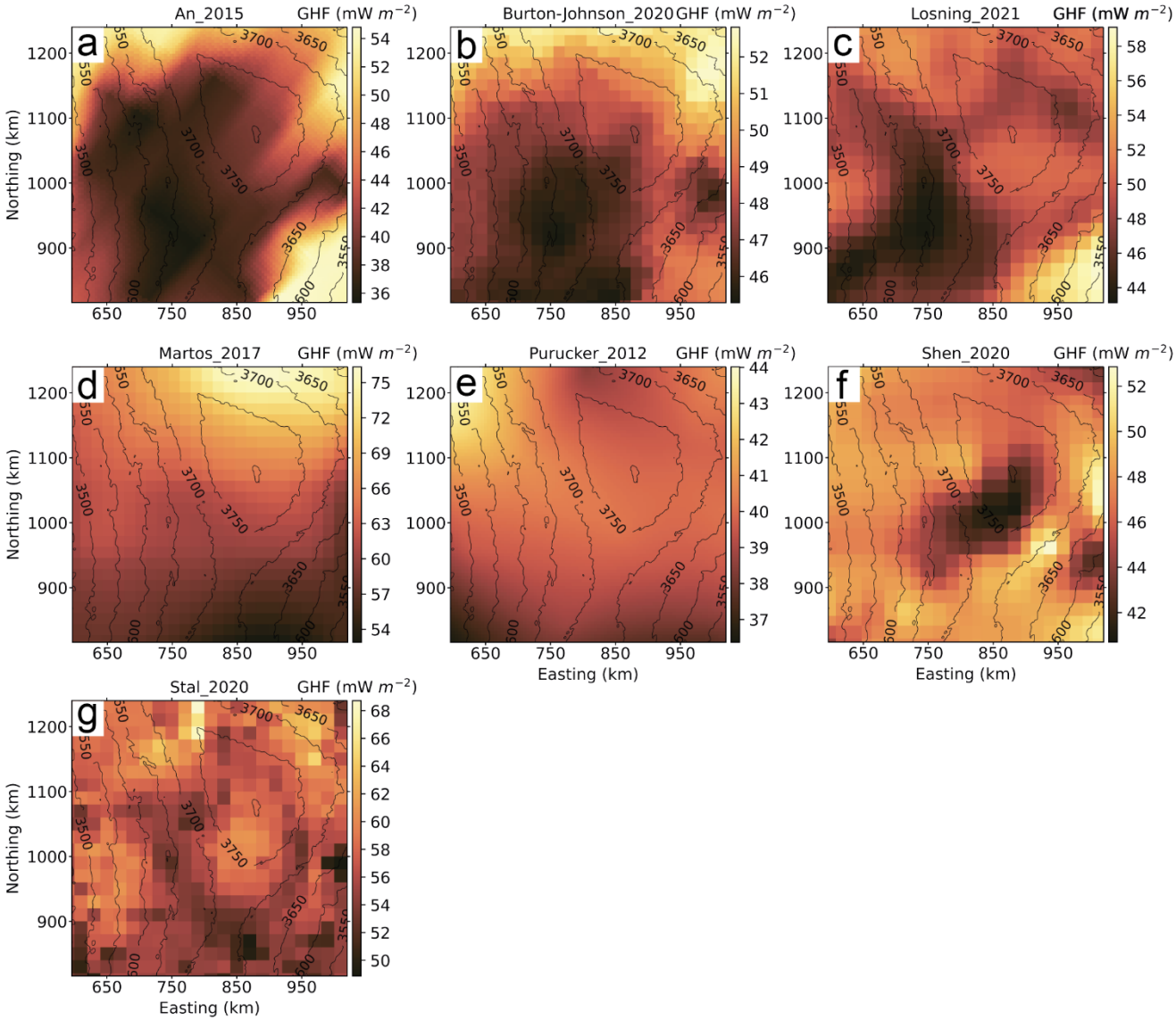

Figure S8: *Modelled pan-Antarctic GHF sampled in the Dome Fuji region* ***a-g)*** *GHF maps labelled with associated publication (Shen et al., 2020; Stål et al., 2020; An et al., 2015; Purucker, 2012; Losning et al., 2021; Martos et al., 2017; Burton-Johnson et al., 2020). Ice surface contours drawn based on REMA* (Howat et al., 2019). *Note: different colour scale ranges due to wide spread of modelled GHF values.*

S3.3 Bed roughness and uncertainty

Table S3: Statistics for linear regression models for Topographic Roughness Index (TRI) and Median Absolute Deviation (MAD).

Interval	Slope	Num. Obs.	RMSE	R^2
0-500	0.15875	85926	16.48698	0.329271
500-1000	0.25018	85004	14.96867	0.631985
1000-1500	0.32147	86489	14.13916	0.760733
1500-2000	0.37367	83717	14.28693	0.804909
2000-2500	0.41035	86320	14.77184	0.820207
2500-3000	0.44275	70812	16.08543	0.806945
3000-3500	0.47691	53239	17.27262	0.790263
3500-4000	0.50429	44616	17.98858	0.780341
4000-4500	0.52426	38351	18.36653	0.77619
4500-5000	0.53870	30809	18.77894	0.769702
5000-5500	0.57396	12751	17.51052	0.794966
5500-6000	0.58995	10759	17.36857	0.786223
6000-6500	0.60165	9543	17.17621	0.789962
6500-7000	0.61033	8328	16.71906	0.787735
7000-7500	0.61304	6229	16.33385	0.770303
7500-8000	0.64085	749	15.50713	0.720789
8000-8500	0.64211	420	14.53889	0.449234
8500-9000	0.65066	249	13.84399	0.30013
9000-9500	0.66853	89	12.28784	0.255493

Additional Supporting Information

Animated ensemble results are provided at https://doi.org/10.21334/npolar.2023.dbd63194 and have the following captions:

Movie S1: Simulated bed topography results (n = 100) as individual hillshaded relief maps animated at 3 frames per second. Ice surface contours drawn at 50 m intervals from Howat et al., (2019).

Movie S2: Topographic adjustments to background geothermal heat flow, based on simulated bed topography results (n = 100). Drawn as individual hillshaded relief maps and animated at 3 frames per second. Ice surface contours drawn at 50 m intervals from Howat et al., (2019).